Microparticle separation using dielectrophoresis-assisted inertial microfluidics: A GPU-accelerated immersed boundary–lattice Boltzmann simulation

Hossein Sorour Amini and Aliasghar Mohammadi[*]

Department of Chemical and Petroleum Engineering, Sharif University of Technology, Tehran 1458889694, Iran

In this study, the migration of microparticles towards the inertial equilibrium positions in a straight microchannel with a square cross section in the presence of an inhomogeneous oscillating electric field was examined. The dynamics of microparticles were simulated using the immersed boundary–lattice Boltzmann method of fluid-structure interaction simulation. Moreover, the lattice Boltzmann Poisson solver was applied to calculate the electric field required for calculation of the dielectrophoretic force using the equivalent dipole moment approximation. These numerical methods were implemented on a single GPU coupled with the AA pattern of storing distribution functions in memory to speed up the computationally demanding simulation of microparticles dynamics. In the absence of an electric field, spherical polystyrene microparticles migrate to four symmetric stable equilibrium positions corresponding to the sidewalls of the square cross-sectional microchannel. The equilibrium distance from the sidewall was increased by increasing the particle size. The equilibrium positions near electrodes disappeared and particles migrated to the other equilibrium positions far from the electrodes by the application of the high-frequency oscillatory electric field at voltages beyond a threshold value. Finally, a two-step dielectrophoresis-assisted inertial microfluidics methodology was introduced for particle separation based on the crossover frequencies and the observed threshold voltages of different particles. The proposed method exploited the synergistic effect of dielectrophoresis and inertial microfluidics methods to remove their limitations, allowing the separation of a broad range of polydisperse particle mixtures with a single device in a short time.

I. INTRODUCTION

The separation of particles and cells has extensive applications in engineering and medicine including blood fractionation, circulating tumor cells detection, and water purification [1]. Centrifugation and filtration are two conventional particle separation methods which suffer from limitations such as the risk of working with high-speed rotating devices, filter clogging, and fouling [2,3]. Microfluidic particle separation methods have recently attracted a considerable deal of attention. Microfluidic particle separation methods include two leading groups of active and passive approaches [4]. While active methods utilize an external force to separate particles, hydrodynamic forces and microchannel structures are the basis of passive separation methods [4].

In active separation methods, the fluid flow rate should be low enough to expose particles to the sufficient amount of external force, leading to low-throughput and a time-consuming separation approach. On the other hand, separation is highly controllable through manipulating the applied external force [5]. Dielectrophoresis, magnetophoresis [6], optophoresis [7], and acoustophoresis [8] are some examples of phenomena generating active forces based on the difference in dielectric properties, magnetic susceptibility, refractive index, and compressibility. Dielectrophoresis refers to the migration of

polarized particles in a nonuniform electric field, which has been extensively employed for label-free separation and manipulation of particles in microfluidic systems. This method can be controlled by voltage and frequency of the applied electric field [9,10].

Conventional dielectrophoresis-based microfluidic separation devices typically work at low flow rates. At high flow rates, hydrodynamic forces acting on the particle are stronger than the dielectrophoretic force and determine the lateral position of the particle. The dielectrophoretic force has a negligible effect on the final position of the particle, especially at the dead electrical field spaces far away from electrodes. Wang *et al.* [11] tried to remove dead electrical field spaces by using electrodes at the left and right walls of the microchannel. Using different frequencies and voltages at electrodes corresponding to each wall, this method increases the controllability of the separation. Although their method increased the separation efficiency, the flow rate was still less than $1 \, \mu l \, min^{-1}$.

In a group of passive separation methods relying on inertial microfluidics, inertial effects (Dean drag and inertial lift forces) act on microparticles and are the basis of particle manipulation. Depending on the microchannel structure, there exist few points at the cross section where the resultant of all forces normal to the flow direction acting on the immersed particle is zero, where the particle is in equilibrium. The number and position of these points depend on the fluid and particle properties and microchannel structure. In these

_____
[*]amohammadi@sharif.edu

methods, separation occurs based on the difference between the equilibrium positions of different particles. High-throughput and fast separation are the advantages of inertial methods as inertial forces increase by increasing the fluid flow rate. Nevertheless, these methods are not easily controllable, and it is practically difficult to design and fabricate a device to separate a broad range of polydisperse particle mixtures [5].

The advantages of each leading group can suppress the disadvantages of the other one, thus, a combination of active and passive methods can be used to overcome the limitations. In this regard, the combination of dielectrophoresis and inertial microfluidics has already been studied [12–14], where the dielectrophoretic force generated from the electrodes located at the bottom of the serpentine microchannel modifies the equilibrium position of particles presorted at the lower part of the microchannel using the sheath flow. Although the configuration provides a high-throughput and controllable separation, the existence of sheath flow which contaminates the processing specimen and the need for continuous exertion of dielectrophoretic force which increases the possibility of cell lysis in the case of bioparticle separation are the main drawbacks.

In this study, the synergistic effect of dielectrophoresis and inertial microfluidics particle separation methods is examined in a straight microchannel to present a high-throughput sheath-less particle separation methodology in which, dielectrophoretic force is only used to switch particles between equilibrium positions at the microchannel cross section. Therefore, the proposed method does not require the continuous exertion of dielectrophoretic force.

To design this hybrid methodology, the dynamics of microparticles in the proposed microchannel have been simulated using the immersed boundary and lattice Boltzmann methods. In the lattice Boltzmann method, macroscale quantities (fluid velocity, density, and electric potential) are calculated using a set of mesoscale probability distribution functions which must be stored in memory along with the macroscale quantities. Thus, the lattice Boltzmann method requires large memory compared to other numerical methods for solving the Navier-Stokes equations which deal only with the macroscale quantities. Moreover, in the immersed boundary method, the mesh or grid size around the immersed object should be sufficiently small to enable accurate simulations; hence, the immersed boundary–lattice Boltzmann simulation of fluid-structure interaction phenomena is computationally expensive.

One solution involves the use of parallel computing. Owing to its several computational cores, calculations by the graphics processing units (GPUs) are much faster than central processing units (CPUs). GPUs, however, suffer from limited memory in comparison with CPUs, necessitating memory management in performing the immersed boundary–lattice Boltzmann calculation by GPUs. In this study, the AA pattern of storing or reading distribution functions in or from memory was utilized in immersed boundary–lattice Boltzmann simulations to enable the fast and efficient simulations of fluid-particle systems. It is noteworthy that the AA memory pattern provides a single lattice streaming method [15] that decreases the required memory of the lattice Boltzmann method to half.

The remainder of this study is organized as follows. The physics behind the inertial migration of microparticles and dielectrophoresis phenomena is explained in the theory section. In the numerical method section, the immersed boundary and lattice Boltzmann methods have been proposed for solving governing differential equations. The inertial focusing of spherical particles and the effect of dielectrophoretic force on the number and location of inertial equilibrium positions are addressed in the results and discussion section. Finally, the separation of different-sized polystyrene microparticles as well as the separation of same-sized CTCs and WBCs by the developed dielectrophoresis-assisted inertial microfluidics approach are simulated.

II. THEORY

Consider a particle in a straight microchannel with a square cross section where the electrodes are located at the walls of the microchannel to generate a nonuniform oscillatory electric field. The inertial migration and electrokinetic phenomena should be considered to investigate the dynamics of the particle. For this purpose, the physics underlying the inertial migration phenomenon is presented in the first part of this section, in which the inertial forces modulating the dynamics of microparticles are explained. Note that the forces originate from the convective terms $(\mathbf{u} \cdot \nabla)\mathbf{u}$ of the Navier-Stokes equation

$$\rho\left[\frac{\partial \mathbf{u}}{\partial t} + (\mathbf{u} \cdot \nabla)\mathbf{u}\right] = \mu\nabla^2\mathbf{u} - \nabla P + \rho\mathbf{g}_d + \mathbf{F}_b, \quad (1)$$

where ρ, $\mathbf{u}$, and P denote fluid density, velocity, and pressure, respectively. $\rho\mathbf{g}_d$ is the force density driving the fluid in the microchannel. $\mathbf{F}_b$ represents the immersed boundary force density, which is used to simulate fluid-particle interaction. The second part of this section is devoted to the equations governing the dielectrophoretic migration of a spherical particle in an oscillatory electric field.

A. Inertial migration

First observed by Segre and Silberberg [16,17], particles dispersed in a channel flow experience inertial forces, concentrating them to specific locations at the channel cross section called equilibrium positions depending on the particle and fluid characteristics as well as channel structure. Of these inertial forces, we can mention wall-induced lift, shear-induced lift, Saffman lift, Magnus, and Dean drag forces (generated by secondary flow in curved microchannels) [18]. Hu and Leal [19] showed that wall- and shear-induced lift forces are dominant inertial forces in a straight microchannel. Wall-induced lift force is assigned to the interaction of the flow field with the particle and confining wall, which repels the suspending particle away from the channel wall. Shear-induced lift force is originated from the interaction of curved fluid velocity profile with the immersed particle, which repels the particle away from the channel center. Various methods have been developed for calculating these forces [20]; the most precise one is fluid-structure interaction simulation. In this study, fluid-structure interaction simulation was utilized

through the immersed boundary method, which includes all the inertial forces at different Reynolds numbers.

B. Dielectrophoresis

Dielectrophoresis refers to a phenomenon in which a nonuniform electric field exerts a net body force on a dielectric particle polarized in the electric field. The net body, so-called dielectrophoretic, force can be calculated by the equivalent dipole moment approximation, in which the polarized particle is addressed—in an approximate manner—as an induced dipole. This assumption is reasonable at regions where the characteristic variation length of the electric field is sufficiently large compared to the particle size [21]. Using equivalent dipole moment approximation, the time-averaged dielectrophoretic force acting on a spherical particle of radius r_p in an oscillatory electric field is calculated as [22]

$$\mathbf{F}_{\text{DEP}} = 2\pi \epsilon_m r_p^3 \text{Re[CM]} \boldsymbol{\nabla} |\mathbf{E}_{rms}|^2, \tag{2}$$

where $\mathbf{E}_{rms}$ is the root-mean-squared value of the electric field and ϵ_m denotes the permittivity of fluid medium surrounding the spherical particle. Re[CM] also indicates the real part of the Clausius-Mossotti factor

$$\text{CM} = \frac{\epsilon_p^* - \epsilon_m^*}{\epsilon_p^* + 2\epsilon_m^*}. \tag{3}$$

Indices p and m denote particle and fluid medium, respectively. ϵ^* represents the complex permittivity given by

$$\epsilon^* = \epsilon - i\frac{\sigma}{\omega}, \tag{4}$$

where σ is the electrical conductivity and $\omega = 2\pi f$ is the angular frequency in which f stands for the frequency of the applied oscillatory electric field.

According to Eq. (2), the sign of Re[CM] determines the direction of the dielectrophoretic force. When Re[CM] > 0, the particle migrates towards regions with a higher value of the electric field, and when Re[CM] < 0, the particle moves towards regions with a lower value of the electric field. In the present study, dielectrophoretic force has been utilized to manipulate inertial equilibrium positions of polystyrene microparticles, large lymphocytes, and MDA-231 cancer cells. The Clausius-Mossotti factors are presented in Appendix C for these particles.

However, $\mathbf{E}_{rms}$ must be determined to calculate the dielectrophoretic force. For this purpose, the electric field distribution is calculated from the electric potential distribution by

$$\mathbf{E} = -\boldsymbol{\nabla}\phi \tag{5}$$

for a domain with uniform permittivity and electrical conductivity. Electric field distribution is related to the charge density distribution (q) through the Gauss law

$$\boldsymbol{\nabla} \cdot \mathbf{E} = \frac{q}{\epsilon}. \tag{6}$$

The Poisson equation governing the electric potential distribution in the microchannel is derived by combining Eqs. (5) and (6),

$$\nabla^2 \phi = -\frac{q}{\epsilon}. \tag{7}$$

When the electrical double layer is very thin and there is no charge in the bulk of fluid, Eq. (7) is simplified to the Laplace equation [23]

$$\nabla^2 \phi = 0. \tag{8}$$

For an oscillatory voltage of $\phi = \phi_p \sin(\omega t)$, the peak voltage ($\phi_p$) is related to the root-mean-squared voltage (ϕ_{rms}) through

$$\phi_{rms}^2 = \frac{1}{T}\int_0^T \phi_p \sin^2(\omega t)\, dt = \frac{\phi_p^2}{2}. \tag{9}$$

Substituting the oscillatory voltage in Eq. (8) and using Eq. (9) leads to

$$\nabla^2 \phi_{rms} = 0. \tag{10}$$

By solving Eq. (10) and calculating ϕ_{rms}, $\mathbf{E}_{rms}$ is determined from Eq. (5) throughout the simulation domain. Then the dielectrophoretic force is calculated by Eq. (2). It must be realized that the electric field is considered to be unperturbed by the presence of the particle; thus, Eq. (10) is solved only once, which significantly reduces the computational cost.

III. NUMERICAL METHODS

The distribution of fluid velocity and electric potential must be determined to investigate the effect of dielectrophoretic force on the inertial migration of microparticles. The lattice Boltzmann method was employed in the present study to solve the governing equations. The details of the lattice Boltzmann method for solving the Navier-Stokes and Poisson equations are presented in the following subsections, followed by the implementation of Dirichlet and Neumann boundary conditions. Subsequently, the immersed boundary method is proposed for the fluid-structure interaction simulation to implement the no-slip condition at the surface of the immersed particle. Finally, some remarks are presented on the selection of simulation parameters and the stability of the simulation.

A. Navier-Stokes solver

D_3Q_{19} lattice Boltzmann method was used to solve the governing equations for the fluid flow. This method solves the discrete form of the Boltzmann equation [24]

$$f_i(\mathbf{x} + \mathbf{e}_i \Delta t, t + \Delta t) = f_i(\mathbf{x}, t) + \Omega_i^f(\mathbf{x}, t)\Delta t + F_i(\mathbf{x}, t)\Delta t, \tag{11}$$

which describes the evolution of distribution functions f_i. According to Eq. (11), distribution functions f_i at point $\mathbf{x}$ and time t are transferred with the lattice velocity vectors $\mathbf{e_i}$ to the neighboring points $\mathbf{x} + \mathbf{e}_i \Delta t$ as one time step elapses. The velocity vectors are depicted in Fig. 1.

Ω_i^f is the collision operator for the rate of change in distribution function f_i due to the elastic collisions of gas particles with different velocities. In the present study, Bhatnagar-Gross-Krook (BGK) collision model was used:

$$\Omega_i^f(\mathbf{x}, t) = -\frac{1}{\tau_f}\big[f_i(\mathbf{x}, t) - f_i^{\text{eq}}(\mathbf{x}, t)\big]. \tag{12}$$

In the BGK model, the distribution functions tend to relax to their equilibrium values f_i^{eq} after time τ_f.
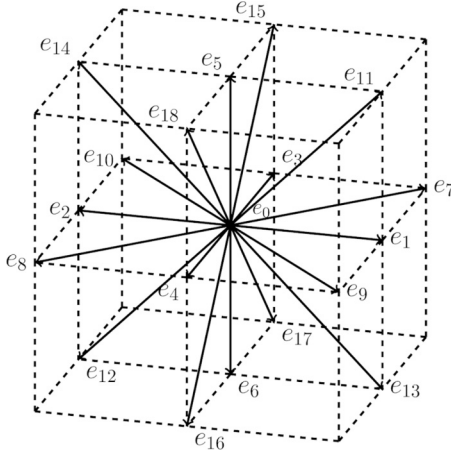
FIG. 1. Discrete velocity vectors of the D_3Q_{19} lattice Boltzmann method.

Using the Chapman-Enskog analysis, τ_f is related to the fluid kinematic viscosity ν as [25]

$$\nu \frac{\Delta t}{\Delta x^2} = c_s^2(\tau_f - 0.5), \tag{13}$$

where $c_s(= 1/\sqrt{3})$ is the speed of sound.

In Eq. (12), f_i^{eq}, the so-called the equilibrium distribution, is the discrete form of the Maxwell-Boltzmann distribution. Using the orthogonality of Hermite polynomials, the Maxwell-Boltzmann distribution is expanded as [24]

$$f_i^{\text{eq}}(\mathbf{x}, t) = w_i \rho(\mathbf{x}, t)\left[1 + \frac{\mathbf{e_i} \cdot \mathbf{u}(\mathbf{x}, t)}{c_s^2} \right.$$
$$\left. + \frac{[\mathbf{e_i} \cdot \mathbf{u}(\mathbf{x}, t)]^2}{2c_s^4} - \frac{\mathbf{u}^2(\mathbf{x}, t)}{2c_s^2}\right], \tag{14}$$

where w_i is the weight coefficient corresponding to the lattice velocity vector $\mathbf{e_i}$, which is defined as

$$w_i = \begin{cases} \frac{1}{3} & i = 0 \\ \frac{1}{18} & i = 2, 3, \ldots, 8 \\ \frac{1}{36} & i = 9, 10, \ldots, 18 \end{cases}. \tag{15}$$

Returning to Eq. (11), F_i is the lattice Boltzmann force model. In the present study, the force model proposed by Guo *et al.* [26] was used:

$$F_i(\mathbf{x}, t) = w_i\left(1 - \frac{1}{2\tau_f}\right)\left[\frac{\mathbf{e_i} - \mathbf{u}(\mathbf{x}, t)}{c_s^2} + \frac{\mathbf{e_i} \cdot \mathbf{u}(\mathbf{x}, t)}{c_s^4}\mathbf{e_i}\right] \cdot \mathbf{f}(\mathbf{x}, t), \tag{16}$$

where $\mathbf{f}$ is the force density exerted on the fluid. In Eqs. (14) and (16) fluid density and velocity are calculated as

$$\rho(\mathbf{x}, t) = \sum_{i=0}^{18} f_i(\mathbf{x}, t), \tag{17}$$

$$\rho\mathbf{u}(\mathbf{x}, t) = \sum_{i=0}^{18} \mathbf{e_i} f_i(\mathbf{x}, t) + \frac{\Delta t}{2}\mathbf{f}(\mathbf{x}, t), \tag{18}$$

which are, respectively, the zeroth- and first-order moments of f_i.

B. Poisson solver

A time derivative term is added to the Poisson equation to solve the elliptic Poisson equation

$$\frac{\partial \phi}{\partial \tilde{t}} = \gamma \nabla^2 \phi + \frac{\gamma q}{\epsilon}, \tag{19}$$

where γ is an arbitrary constant. We employed a new distribution function to solve Eq. (19) with the D_3Q_{19} lattice Boltzmann method [27]:

$$g_i(\mathbf{x} + \mathbf{e_i}\Delta\tilde{t}, \tilde{t} + \Delta\tilde{t}) = g_i(\mathbf{x}, \tilde{t}) + \Omega_i^g(\mathbf{x}, \tilde{t})\Delta\tilde{t} + Q_i(\mathbf{x}, \tilde{t})\Delta\tilde{t}. \tag{20}$$

It must be noted that the steady-state solution of Eq. (19) is the same as the solution of the Poisson equation. $\tilde{t}$ in Eq. (19) does not represent the real time and is only introduced to solve the Poisson equation. Ω_i^g is the BGK collision operator:

$$\Omega_i^g(\mathbf{x}, \tilde{t}) = -\frac{1}{\tau_g}\left[g_i(\mathbf{x}, \tilde{t}) - g_i^{\text{eq}}(\mathbf{x}, \tilde{t})\right]. \tag{21}$$

In the BGK collision model, τ_g is the relaxation time, which is related to γ as [25]

$$\gamma \frac{\Delta\tilde{t}}{\Delta x^2} = c_s^2(\tau_g - 0.5). \tag{22}$$

In Eq. (21) g_i^{eq} is the equilibrium distribution function

$$g_i^{\text{eq}}(\mathbf{x}, \tilde{t}) = w_i\phi(\mathbf{x}, \tilde{t}). \tag{23}$$

Returning to Eq. (20), $Q_i(\mathbf{x}, \tilde{t})$ shows the source term [27]

$$Q_i(\mathbf{x}, \tilde{t}) = w_i\left(1 - \frac{1}{2\tau_g}\right)\frac{\gamma q(\mathbf{x}, \tilde{t})}{\epsilon}. \tag{24}$$

Also, electric potential ϕ is determined by

$$\phi(\mathbf{x}, \tilde{t}) = \sum_{i=0}^{18} g_i(\mathbf{x}, \tilde{t}) + \frac{\Delta\tilde{t}}{2}\frac{\gamma q(\mathbf{x}, \tilde{t})}{\epsilon} \tag{25}$$

as the zeroth moment of g_i.

C. Boundary conditions

Each time step of the lattice Boltzmann method is regarded as the collision [Eqs. (26) and (27)] and propagation [Eqs. (28) and (29)] steps:

$$f_i^*(\mathbf{x}, t) = f_i(\mathbf{x}, t) + \Omega_i^f(\mathbf{x}, t)\Delta t + F_i(\mathbf{x}, t)\Delta t, \tag{26}$$

$$g_i^*(\mathbf{x}, \tilde{t}) = g_i(\mathbf{x}, \tilde{t}) + \Omega_i^g(\mathbf{x}, \tilde{t})\Delta\tilde{t} + Q_i(\mathbf{x}, \tilde{t})\Delta\tilde{t}, \tag{27}$$

$$f_i(\mathbf{x} + \mathbf{e_i}\Delta t, t + \Delta t) = f_i^*(\mathbf{x}, t), \tag{28}$$

$$g_i(\mathbf{x} + \mathbf{e_i}\Delta\tilde{t}, \tilde{t} + \Delta\tilde{t}) = g_i^*(\mathbf{x}, \tilde{t}), \tag{29}$$

where f_i^* and g_i^* are postcollision, as well as f_i and g_i are postpropagation distribution functions. In each time step, distribution functions propagating into the boundaries of the computational domain are unknown and must be determined by the lattice Boltzmann boundary condition methods.

We have used the bounce-back method to implement the no-slip boundary condition at the channel walls of the developed Navier-Stokes solver. For this purpose, computational

nodes (cubic lattice nodes) are distributed in the fluid domain such that the physical boundary is placed in the middle of the lattice nodes to ascertain second-order accuracy [24]. In this way, the bounce-back method is applied to the postpropagation distribution functions as [28]

$$f_i(\mathbf{x_b}, t + \Delta t) = f_{-i}(\mathbf{x_b} - \mathbf{e_i}\Delta t, t + \Delta t), \quad (30)$$

where $\mathbf{x}_b$ is the coordinates of the lattice nodes adjacent to the physical boundary. Index i denotes the directions of lattice velocity vectors corresponding to the unknown distribution functions for which the boundary condition must be enforced and $-i$ is the direction opposite to i. Moreover, the bounce-back method, which was employed for the postcollision distribution functions, is

$$f_i^*(\mathbf{x_b} - \mathbf{e_i}\Delta t, t) = f_{-i}^*(\mathbf{x_b}, t). \quad (31)$$

In addition, the nonequilibrium extrapolation method was used to implement the Dirichlet and Neumann boundary conditions for solving the Poisson equation using the lattice Boltzmann method. For this purpose, the physical boundary is located on the first computational node $\mathbf{x}_b$. In this regard, the nonequilibrium extrapolation method is applied to the postpropagation distribution functions as [29]

$$g_i(\mathbf{x}_b, \tilde{t} + \Delta\tilde{t}) = g_i^{eq}(\mathbf{x}_b, \tilde{t} + \Delta\tilde{t}) + g_i^{neq}(\mathbf{x}_f, \tilde{t} + \Delta\tilde{t}), \quad (32)$$

where $\mathbf{x}_f$ is the first fluid node adjacent to the boundary node $\mathbf{x}_b$. The nonequilibrium part of the distribution function is equal to the difference between the postpropagation distribution function and equilibrium distribution function ($g_i^{neq} = g_i - g_i^{eq}$). In the case of a Neumann boundary condition, the electric potential required to obtain $g_i^{eq}(\mathbf{x_b}, \tilde{t} + \Delta\tilde{t})[= w_i\phi(\mathbf{x_b}, \tilde{t} + \Delta\tilde{t})]$ at the boundary node is calculated using the extrapolation from fluid values. Furthermore, the nonequilibrium extrapolation method was applied to the postcollision distribution functions as

$$g_i^*(\mathbf{x}_b - \mathbf{e}_i\Delta\tilde{t}, \tilde{t}) = g_i^{eq}(\mathbf{x}_b, \tilde{t} + \Delta\tilde{t}) + g_i^*(\mathbf{x}_f - \mathbf{e}_i\Delta\tilde{t}, \tilde{t})$$
$$- w_i\sum_{j=0}^{j=18} g_j^*(\mathbf{x}_f - \mathbf{e}_j\Delta\tilde{t}, \tilde{t}). \quad (33)$$

In the case of Dirichlet boundary condition, the value of $g_i^{eq}(\mathbf{x_b}, \tilde{t} + \Delta\tilde{t})[= w_i\phi(\mathbf{x_b}, \tilde{t} + \Delta\tilde{t})]$ is known at the boundary node. In the case of a Neumann boundary condition, however, the electric potential should be obtained for $g_i^{eq}(\mathbf{x_b}, \tilde{t} + \Delta\tilde{t})$ using the extrapolation from fluid values at time $\tilde{t}$ as

$$\phi(\mathbf{x_b}, \tilde{t} + \Delta\tilde{t}) = \sum_{j=0}^{j=18} g_j^*(\mathbf{x}_f - \mathbf{e}_j\Delta\tilde{t}, \tilde{t}). \quad (34)$$

D. Immersed boundary method

As previously stated, the fluid-structure interaction simulation allows for precise simulation of the inertial migration phenomena. In this study, immersed boundary method was used to simulate fluid-structure interaction; in which the linear and angular momentums transferred from the fluid to the particle lead to the translational and rotational motion of the particles. The linear momentum balance governs the

translational motion of a solid particle suspended in a fluid [30]:

$$m_p\frac{d\mathbf{U}_p}{dt} = \int_{CS}(\boldsymbol{\sigma}\cdot\mathbf{n})\,ds + (\rho_p - \rho_f)V_p\mathbf{g} + \mathbf{F}_{\text{DEP}}, \quad (35)$$

where m_p, V_p, and ρ_p are the particle mass, volume, and density, respectively. ρ_f also shows the fluid density and $\boldsymbol{\sigma}$ $(= \mu[\nabla\mathbf{u} + (\nabla\mathbf{u})^T] - P\boldsymbol{\delta}$ with $\boldsymbol{\delta}$ the identity tensor) denotes the fluid stress tensor. The first term on the right side of Eq. (35) shows the interaction between the surrounding fluid and the particle, while the second term arises from the net buoyancy force acting on the particle.

In the immersed boundary method, the momentum transfer between fluid and particle is modeled using the force terms in the fluid and particle momentum equations. In this regard, the suspended solid particle is replaced with a very thin fluid-loaded shell. Subsequently, the imaginary surface force density $\mathbf{F_s}$ is imposed to move the imaginary shell with the same velocity as the solid particle

$$m_f\frac{d\mathbf{U}_p}{dt} = \int_{CS}(\boldsymbol{\sigma}\cdot\mathbf{n})\,ds + \int_{CS}\mathbf{F}_s\,ds, \quad (36)$$

where $m_f = V_p\rho_f$. Using Eq. (36), Eq. (35) is rewritten as

$$m_p\frac{d\mathbf{U_p}}{dt} = -\int_{CS}\mathbf{F_s}\,ds + (\rho_p - \rho_f)V_p\mathbf{g} + m_f\frac{d\mathbf{U_p}}{dt} + \mathbf{F}_{\text{DEP}}. \quad (37)$$

In addition, discretization of Eq. (37) results in

$$\mathbf{U}_p(t + \Delta t) = \mathbf{U}_p(t) - \frac{\Delta t}{m_p}\left[\sum_s \mathbf{F}_s(\mathbf{x}_s, t)\Delta S\right]$$
$$+ \left(1 - \frac{\rho_f}{\rho_p}\right)\mathbf{g}\Delta t + \frac{\rho_f}{\rho_p}[\mathbf{U_p}(t) - \mathbf{U_p}(t - \Delta t)]$$
$$+ \frac{\Delta t}{m_p}\mathbf{F}_{\text{DEP}}, \quad (38)$$

where $\mathbf{x}_s$ shows the location of computational nodes at the particle surface. The particle center of mass position $\mathbf{x}_c$ is updated as

$$\mathbf{x}_c(t + \Delta t) = \mathbf{x}_c(t) + \tfrac{1}{2}[\mathbf{U}_p(t + \Delta t) + \mathbf{U}_p(t)]. \quad (39)$$

Similarly, the angular momentum balance governing the rotational motion of the particle is

$$I_p\frac{\boldsymbol{\Omega}_p^B}{dt} = \int_{CS}(\mathbf{x} - \mathbf{x}_c)^B \times (\boldsymbol{\sigma}\cdot\mathbf{n})^B\,ds, \quad (40)$$

where $\boldsymbol{\Omega}_p^B$ is the particle angular velocity. I_p denotes the particle moment of inertia ($I_p = 0.4\rho_p V_p r_p^2$ for spherical particle). The superscript B indicates the body-fixed reference frame. By introducing the surface force density $\mathbf{F}_s$, Eq. (40) is simplified to

$$I_p\frac{d\boldsymbol{\Omega}_p^B}{dt} = -\int_{CS}(\mathbf{x} - \mathbf{x}_c)^B \times \mathbf{F}_s^B\,ds + I_f\frac{d\boldsymbol{\Omega}_p^B}{dt}, \quad (41)$$

where I_f shows the moment of inertia for the thin fluid-loaded spherical shell ($I_f = 0.4\rho_f V_p r_p^2$). Discretization of Eq. (41)

leads to

$$\mathbf{\Omega}_p^B(t + \Delta t) = \mathbf{\Omega}_p^B(t) - \frac{\Delta t}{I_p}\left[\sum_s (\mathbf{x}_s - \mathbf{x}_c)^B \times \mathbf{F}_s^B(\mathbf{x}_s, t)\Delta S\right] + \frac{\rho_f}{\rho_p}\left[\mathbf{\Omega}_p^B(t) - \mathbf{\Omega}_p^B(t - \Delta t)\right]. \tag{42}$$

The unit quaternion $\mathbf{Q}[=(q_0, q_1, q_2, q_3)^T]$ is used to express the particle orientation, where $q_0^2 + q_1^2 + q_2^2 + q_3^2 = 1$. Using $\mathbf{\Omega}_p^B(t + \Delta t)[=(\Omega_x, \Omega_y, \Omega_z)^T]$, calculated from Eq. (42), the quaternion is updated as

$$\mathbf{Q}(t + \Delta t) = \mathbf{Q}(t) + \frac{1}{2}\begin{bmatrix} 0 & -\Omega_x & -\Omega_y & -\Omega_z \\ \Omega_x & 0 & \Omega_z & -\Omega_y \\ \Omega_y & -\Omega_z & 0 & \Omega_x \\ \Omega_z & \Omega_y & -\Omega_x & 0 \end{bmatrix}\mathbf{Q}(t). \tag{43}$$

Equation (42) is written in the body-fixed reference frame where $\mathbf{F}_s^B$ is defined, while Eq. (38) is written in the Eulerian reference frame where $\mathbf{F}_s$ is defined. $\mathbf{F}_s$ is transformed into the body-fixed reference frame using [31]

$$\mathbf{F}_s^B = S\mathbf{F}_s, \tag{44}$$

where S is the rotation matrix

$$S = \begin{bmatrix} q_0^2 + q_1^2 - q_2^2 - q_3^2 & 2(q_1q_2 + q_0q_3) & 2(q_1q_3 - q_0q_2) \\ 2(q_1q_2 - q_0q_3) & q_0^2 - q_1^2 + q_2^2 - q_3^2 & 2(q_2q_3 + q_0q_1) \\ 2(q_1q_3 + q_0q_2) & 2(q_2q_3 - q_0q_1) & q_0^2 - q_1^2 - q_2^2 + q_3^2 \end{bmatrix}. \tag{45}$$

The surface force density in Eqs. (37) and (41) changes the velocity distribution around the particle surface, fulfilling the no-slip boundary condition. The value of this force density at the location of immersed boundary nodes, $\mathbf{x}_s$, is calculated by [32,33]

$$F_s(\mathbf{x}_s, t) = 2\rho(\mathbf{x}_s, t)\frac{\mathbf{U}^d(\mathbf{x}_s, t) - \mathbf{U}^*(\mathbf{x}_s, t)}{\Delta t}\Delta x, \tag{46}$$

where $\mathbf{U}^d$ is the desired velocity of boundary nodes which is calculated in each time step using

$$\mathbf{U}^d(\mathbf{x_s}, t) = \mathbf{U}_p(t) + S^{-1}\left[\mathbf{\Omega}_p^B(t) \times (\mathbf{x_s} - \mathbf{x_c})^B\right], \tag{47}$$

where S^{-1} is the inverse of the rotation matrix, which transforms the quantity into the Eulerian reference frame where $\mathbf{U}_p$ is defined as

$$S^{-1} = \begin{bmatrix} q_0^2 + q_1^2 - q_2^2 - q_3^2 & 2(q_1q_2 - q_0q_3) & 2(q_1q_3 + q_0q_2) \\ 2(q_1q_2 + q_0q_3) & q_0^2 - q_1^2 + q_2^2 - q_3^2 & 2(q_2q_3 - q_0q_1) \\ 2(q_1q_3 - q_0q_2) & 2(q_2q_3 + q_0q_1) & q_0^2 - q_1^2 - q_2^2 + q_3^2 \end{bmatrix}. \tag{48}$$

In Eq. (46), $\mathbf{U}^*$ is the unforced velocity at the boundary node, which is calculated by interpolation of the velocity field calculated by the lattice Boltzmann method

$$\mathbf{U}^*(\mathbf{x}_s, t) = \sum_x \mathbf{u}^*(\mathbf{x}, t)D(\mathbf{x} - \mathbf{x}_s)\Delta x^3, \tag{49}$$

where $\mathbf{u}^*$ is calculated using Eqs. (17) and (18) by setting $\mathbf{f} = \rho\mathbf{g}_d$, where $\rho\mathbf{g}_d$ is the force density driving the fluid. D is the discrete form of the Dirac delta function

$$D(\mathbf{x}) = \frac{1}{\Delta x^3}\mathscr{D}\left(\frac{x}{\Delta x}\right)\mathscr{D}\left(\frac{y}{\Delta x}\right)\mathscr{D}\left(\frac{z}{\Delta x}\right), \tag{50}$$

where $\mathscr{D}$ is given by

$$\mathscr{D}(r) = \begin{cases} \frac{1}{8}(3 - 2|r| + \sqrt{1 + |r| - 4r^2}) & r \leqslant 1 \\ \frac{1}{8}(5 - 2|r| - \sqrt{-7 + 12|r| - 4r^2}) & 1 \leqslant r \leqslant 2 \\ 0 & 2 \leqslant r \end{cases}. \tag{51}$$

The calculated immersed boundary force is distributed to the fluid nodes near the boundary nodes using

$$\mathbf{F}_b(\mathbf{x}, t) = \sum_{\mathbf{x}_s} \mathbf{F}_s(\mathbf{x}_s, t)D(\mathbf{x} - \mathbf{x}_s)\Delta S, \tag{52}$$

where ΔS is the surface area corresponding to each boundary node. The fluid velocity around the boundary is modified using Eq. (18) by setting $\mathbf{f} = \rho\mathbf{g}_d + \mathbf{F}_b$.

E. Simulation details

To solve the governing equations using the lattice Boltzmann method, simulation parameters must be first determined. These parameters include driving force density $\rho\mathbf{g}_d$, lattice spacing Δx, time increment Δt, and relaxation time τ (τ_f and τ_g). The driving force density $\rho\mathbf{g}_d$ in Eq. (1) is calculated as [34]

$$\rho\mathbf{g}_d = \left(\frac{H^4}{12Q\rho_f\nu}\left\{1 - \frac{192}{\pi^5}\sum_{n=0}^{\infty}\frac{1}{(2n+1)^5}\tanh\left[(2n+1)\frac{\pi}{2}\right]\right\}\right)^{-1}\hat{\mathbf{i}}, \tag{53}$$

where ρ_f and ν are density and kinematic viscosity of the Newtonian fluid, respectively. Q is the fluid flow rate in a straight channel with a square cross section of side length H.

According to Eqs. (13) and (22), only two of the three parameters Δx, Δt, and τ can be independently determined. In this study, the values of Δx and τ were set. The value of Δt was calculated using Eqs. (13) and (22). Lattice spacing, Δx, and time increment, Δt, must be sufficiently small to guarantee the accuracy of the simulation. These parameters must also guarantee the stability of the numerical simulation. To guarantee a stable simulation, relaxation time must not be too close to 0.5 while the maximum nondimensional fluid velocity must be less than 0.2 [24],

$$\frac{u_{\max}\Delta t}{\Delta x} \leqslant 0.2, \tag{54}$$

where the maximum velocity occurs at the center of the square cross section

$$u_{\max} = \sum_{n=0}^{\infty}\frac{4g_dH^2}{\nu\pi^3}\frac{1}{(2n+1)^3}\left\{1 - \frac{1}{\cosh}\left[(2n+1)\frac{\pi}{2}\right]\right\}\sin\left[(2n+1)\frac{\pi}{2}\right]. \tag{55}$$

The lattice spacing, Δx, was set to 0.5 μm to ensure grid independency. The relaxation time for the Navier-Stokes solver, τ_f, was also set at 0.7. Using Eq. (13), the time step is calculated as 1.94×10^{-8} s. According to Eq. (53), the driving force density was set 1.897×10^7 N m^{-3} to ascertain a fluid flow rate of 250 μl min^{-1}, which was the opted flow rate in all our simulations. Using Eq. (55), the maximum fluid velocity, $u_{\max}$, was calculated to be 3.493 m s^{-1}, which satisfies the stability condition given in Eq. (54). The relaxation time for the Poisson solver, τ_g, was set to 0.9; thus, according to Eq. (22), the imaginary time step, $\Delta\tilde{t}$, was obtained to be 3.3×10^{-8} s.

In fluid-structure interaction simulation, the lattice spacing must be small enough to resolve the details of the particle surface. According to Eq. (54), by reducing the lattice spacing Δx, the time increment Δt should also be reduced to guarantee the stability of the calculations, which further increases the computational cost. In the present study, parallel computing using GPUs was used for the intensive calculations of the immersed boundary–lattice Boltzmann simulation. Thanks to their many computational cores, GPUs are much faster than CPUs. Therefore, the application of GPUs significantly speeds up the computations for cost-demanding three-dimensional simulations. One constraint in the use of GPUs lies in their limited memory compared to CPUs, further highlighting the necessity of memory management, especially in the memory-hungry lattice Boltzmann method.

AA pattern of storing distribution functions refers to the smart use of memory by combining two successive time steps of the lattice Boltzmann method into a collision and a propagation-collision-propagation steps and changing the sequence of storing distribution functions in memory after these steps [15]. AA memory pattern, in combination with the GPU implemented immersed boundary and lattice Boltzmann methods, facilitates faster and more-involved simulations.

C++ and CUDA API are used to develop the parallel double-precision solver. The details of the simulation algorithm are presented in Appendix A, followed by the validation of the developed solvers in Appendix B. The first step of the algorithm and the dielectrophoretic force calculation method were validated by comparing the numerical and analytical solution of the Poisson equation and the dielectrophoretic force. To validate the developed immersed boundary–lattice Boltzmann code, sedimentation of a single spherical particle was simulated in fluids of different properties. The numerical results were also compared with the previously published experimental data.

IV. RESULTS AND DISCUSSION

The aim of this study is to introduce a robust microparticle separation method utilizing the synergistic effect of the hydrodynamic and electric phenomena. In this regard, the hydrodynamic response of different-sized particles is first examined to determine their migration pattern to the equilibrium positions. In the second part of this section, the dielectrophoretic force is applied to the particles to manipulate their equilibrium positions. The effect of voltage and frequency of the applied electric field on the final position of the particle is also explored. It has been demonstrated that the number and location of the equilibrium positions in the microchannel can be modulated by the applied electric field at specific voltages and frequencies. Thus, a hybrid microparticle separation methodology is proposed based on our results. The separation of microparticles in two challenging particle mixtures is numerically simulated to examine the robustness of the proposed method.

A. Inertial focusing pattern in a square microchannel

The inertial focusing patterns of 5 and 8 μm particles were determined in a straight microchannel [Fig. 2(a)] using the
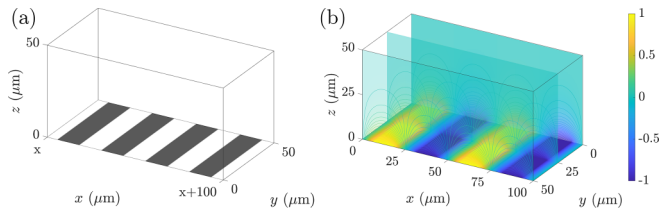
FIG. 2. The geometry of one period of the straight microchannel and the configuration of microelectrodes at the bottom wall for investigating the dielectrophoretic manipulation of inertial equilibrium positions (a), and the distribution of nondimensional electric potential in one simulated period of the straight microchannel (b).

immersed boundary and lattice Boltzmann methods. For this purpose, the no-slip boundary condition was implemented at the microchannel walls using the bounce-back method. Moreover, the periodic boundary condition was used for both particle and fluid along the flow direction.

Figure 3(a) demonstrates the position of a 5 μm particle at the microchannel cross section as a function of time for different initial positions. Additionally, Fig. 3(b) depicts the cross-sectional view of the migration process. It is observed that the particles migrate to four equilibrium positions close to

the center of each microchannel confining wall. When the particle is close to the channel wall, the dominant wall-induced lift force repels the particle away from the wall towards the equilibrium position. On the other hand, when the particle is close to the channel center, the dominated shear-induced lift force leads to the migration of the particle towards the microchannel walls. However, the equilibrium position of a particle depends on its initial position. In this regard, each of the four equilibrium positions corresponds to one of the four isosceles right triangles made by the diagonals of the microchannel cross section. Particles with the initial position in each triangle section migrate to the equilibrium position corresponding to the same section.

According to Figs. 3(a) and 3(b), the migration to the equilibrium positions occurs in two stages, which has already been reported (see [35] and references therein). In stage I, both wall- and shear-induced lift forces govern the migration of particles towards channel walls. In this stage, the net effect of wall- and shear-induced lift forces results in rapid migration of the particles towards a curve, which is a squircle shape as shown in Fig. 3(b). In stage II, due to the rotation-induced lift force, particles follow the minimum lift force curve to the final four equilibrium positions. This two-stage migration process also validates our developed fluid-structure interaction solver

(a) 5 μm particle, 3D view

(b) 5 μm particle, cross-sectional view

(c) 8 μm particle, 3D view

(d) 8 μm particle, cross-sectional view
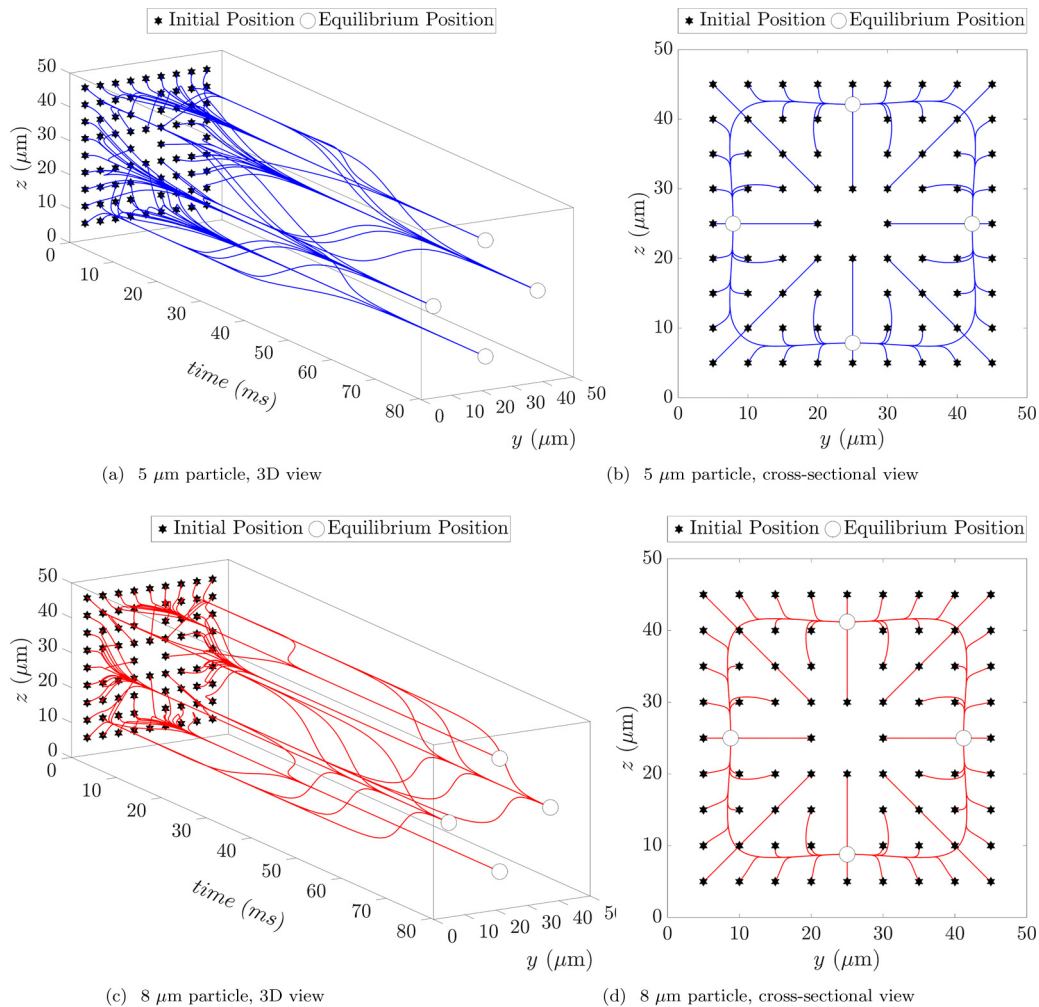
FIG. 3. Inertial focusing pattern of 5 and 8 μm particles in the microchannel of Fig. 2(a).
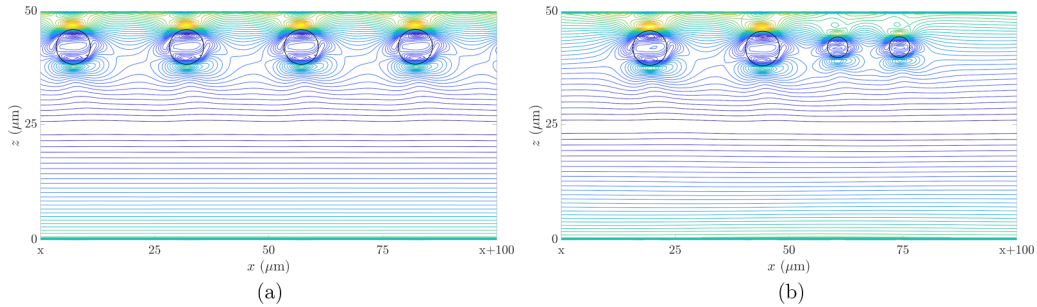
FIG. 4. Vorticity contours around same-sized 8 μm particles (a). Vorticity contours around different-sized particles of 5 and 8 μm diameters (b). Contours are plotted at the plane perpendicular to the top and bottom walls of Fig. 2(a) at $y = 25$ μm.

in addition to the other validations presented in this work. Furthermore, Figs. 3(c) and 3(d) demonstrate the migration process of an 8 μm particle towards equilibrium positions for different initial positions. This particle migrates slower than the 5 μm particle.

Thus far, the dynamics of a solely single particle within a channel flow has been examined. When two or more particles are present in a channel flow, they may interact through the suspending medium leading to the emergence of new phenomena [36,37]. To account partly for the migration of particles within many-body suspensions in a channel flow, two scenarios were simulated to investigate the hydrodynamic interactions of the particles at the inertial equilibrium positions.

In the first scenario, the inertial migration of four 8 μm particles was simulated. The initial position of each particle in the cross section was inside the isosceles right triangle corresponding to the upper wall. Figure 4(a) shows the vorticity contours around 8 μm particles in the plane perpendicular to the top and bottom walls at $y = 25$ μm. The same-sized particles have migrated to the equilibrium position corresponding to the top wall. This observation was expected from the results revealed in Fig. 3.

A train of particles is, however, formed at the equilibrium position. This phenomenon is associated with a two-step dynamics. In the first step, they migrate to the inertial equilibrium position governed by the inertial forces. Afterwards, they continue their motion in the flow direction as the second step. In this step, a repulsive force acts between the adjacent particles, which prevents them from approaching each other. The repulsive force is of the similar nature to the wall-induced lift force, which prevents particles from approaching the wall.

In the second scenario, the inertial migration of two 5 μm as well as two 8 μm particles was simulated. The initial position of the particles at the cross section was inside the isosceles right triangle corresponding to the top wall. According to the results illustrated in Fig. 4(b), the different-sized particles also migrate to the equilibrium position corresponding to the top wall and form a train in the flow direction. In this scenario, the different-sized particles experience different drag forces, which modulates their equilibrium distance in the flow direction. Furthermore, the surface-to-surface distance of two adjacent particles is approximately equal to the sum of their corresponding diameters. This fact is associated with the impact of the particles on the far-field fluid hydrodynamics, which vanishes for distances beyond the particle size [38].

Returning to Fig. 3, a comparison of Figs. 3(b) and 3(d) indicates that the equilibrium positions of the 8 μm particle are slightly closer to the channel centerline than those of the 5 μm particle. Such a negligible difference cannot be used to separate these particles. For separation purposes, it is required to increase the difference by introducing new forces on the particles.

In this regard, different strategies can be adopted including the use of a passive force. For example, an introduction of a curvature into the microchannel geometry generates Dean vortices, leading to Dean drag force on the particles changing their equilibrium positions. The manipulating force can also be an active force generated from external electric, magnetic, or acoustic fields. In the following, the dielectrophoretic force acting on particles is utilized in an oscillatory electric field to manipulate the equilibrium positions and increase the difference between the equilibrium positions of different-sized particles.

B. Dielectrophoretic control of inertial equilibrium positions

Figure 2(b) demonstrates the contours of dimensionless electric potential in one period of the simulated microchannel [Fig. 2(a)]. Dirichlet boundary conditions of $+1$ and -1 V were alternately applied at the electrodes located at the bottom wall using the nonequilibrium extrapolation method. The periodic boundary condition was used in the horizontal direction. A Neumann boundary condition of electric insulation was also applied at the other boundaries using the nonequilibrium extrapolation method [25]. The density and magnitude of the electric potential contours approach zero by increasing the distance from the electrodes.

According to Eq. (2), the real part of the Clausius-Mossotti factor determines the direction of the dielectrophoretic force. In this context, Fig. 5(a) demonstrates the real part of the Clausius-Mossotti factor for the 5 and 8 μm polystyrene particles as a function of electric field frequency. It is observed that the real part of the Clausius-Mossotti factor for the 8 μm particle is zero at the crossover frequency, which is $\sim$170 kHz. Similarly, the crossover frequency of the 5 μm particle is $\sim$290 kHz. At frequencies less than the crossover frequency, the real part of the Clausius-Mossotti factor is positive for the polystyrene microparticles, and the dielectrophoretic force is towards the electrodes. Conversely, at frequencies higher than the crossover frequency, the real part of the Clausius-Mossotti factor for the polystyrene microparticle is
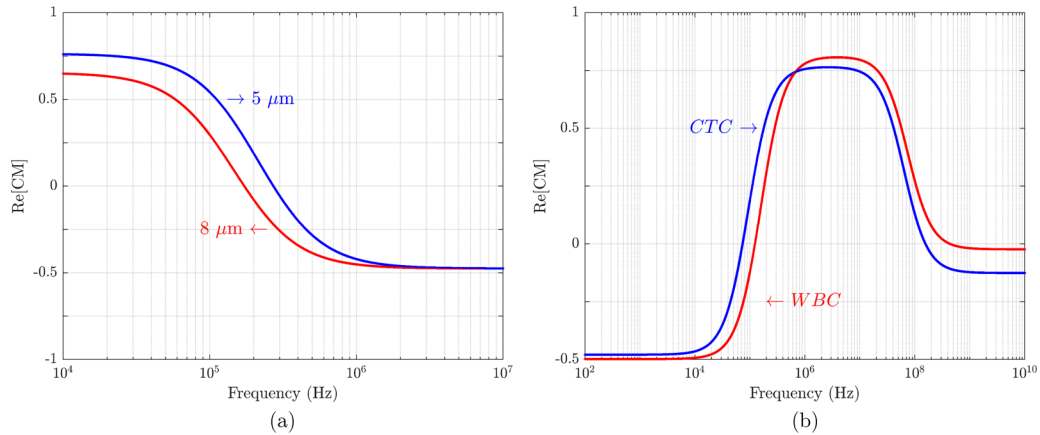
FIG. 5. The real part of the Clausius-Mossotti factor for 5 and 8 μm polystyrene microparticles (a) as well as MDA-231 CTC and lymphocytes white blood cells (b) as a function of the applied electric field frequency.

negative, and the dielectrophoretic force is directed away from electrodes.

Figure 6 demonstrates the migration of 5 and 8 μm polystyrene particles towards equilibrium positions in the presence of dielectrophoretic force generated from the electrodes at the bottom wall of the microchannel [Fig. 2(b)]. At low frequencies [Figs. 6(a) and 6(b)], the polystyrene microparticles experience a positive dielectrophoretic force causing the equilibrium position to approach the bottom wall. Increasing the voltage reduces the distance between the equilibrium position and the wall. As the particle approaches the wall, the value of the upward net lift force opposing the positive dielectrophoretic force is increased.

At high electric field frequencies, the particles experience a negative dielectrophoretic force [Figs. 6(c) and 6(d)]. In this case, the magnitude of the upward dielectrophoretic force increases by increasing the applied voltage from 5 to 25 V, which displaces the equilibrium position corresponding to the bottom wall away from the electrodes [Figs. 6(e) and 6(f)]. Further increase of the voltage [Figs. 6(g) and 6(h)] leads to a threshold voltage at which dielectrophoretic force dominates over the opposing shear-induced lift force, and the corresponding particle passes the channel centerline. The threshold voltage for this configuration ranges from 25 to 30 V. After passing the channel centerline, the shear-induced lift force changes its direction and boosts the dielectrophoretic force to displace the particle away from the channel centerline towards the original equilibrium position corresponding to the top wall, where the resultant of all inertial forces on the particle normal to the flow direction is zero.

According to Fig. 6, in the case of negative dielectrophoresis, the equilibrium positions corresponding to the side walls are slightly displaced upward, while the equilibrium position corresponding to the top wall remains almost intact by the dielectrophoretic force generated from the electrodes located at the bottom wall. The reason could be the short-range nature of the dielectrophoretic force, which exponentially decays by the distance from the electrodes [13].

Before addressing the dielectrophoresis-assisted separation of microparticles, we briefly digress to compare dielectrophoretic and inertial effects that address the dynamics of microparticles within the straight microchannel. To this end,

the dielectrophoretic and inertial migration velocities of a 5 μm particle were calculated in two distinct situations. In all the simulations, the particle was initially located at $y = 25$ μm, leading to the centerline symmetry and, in turn, zero velocity for the particle in the y direction. As such, the particle was able to move only in the x and/or z directions. The particle velocity in the z direction is, however, a measure of the dielectrophoretic and inertial effects.

To investigate the dielectrophoretic effects, the particle was initially located at $z = 5$ μm. The frequency of the applied electric potential was fixed at 100 MHz such that the particle was experiencing a negative dielectrophoretic force. The simulations were performed at the voltages of 5, 10, 15, 20, 25, and 30 V. Moreover, the driving force was absent to ensure the solely dielectrophoretic-driven particle motion.

In addition, other simulations were performed for four different initial vertical distances of $z = 5$, 24.9, 25.1, and 45 μm to investigate the inertial effects. For these simulations, the voltage was fixed at 0 V to ensure the solely flow rate-driven particle motion.

Figure 7 shows the z component of the particle velocity for the two aforementioned distinct simulations. The particle velocity increases under the influence of inertial forces. The particle velocity asymptotes to zero by approaching the equilibrium positions. A comparison of the dielectrophoretic and inertial migration velocities indicates that the dielectrophoretic effects are dominant near the electrodes. By increasing the distance from electrodes, the dielectrophoretic effects exponentially decay [13] such that dielectrophoretic effects disappear beyond 30 μm distance from the electrodes.

C. Dielectrophoresis-assisted separation of microparticles

It was observed in the previous section that a strong negative dielectrophoretic force releases trapped particles from inertial equilibrium positions in the vicinity of electrodes. As the dielectrophoretic force is highly controllable through the voltage and frequency of the applied electric field, it is possible to displace target particles to specific equilibrium positions using the controllable negative dielectrophoretic force for their complete separation from the nontarget particles.
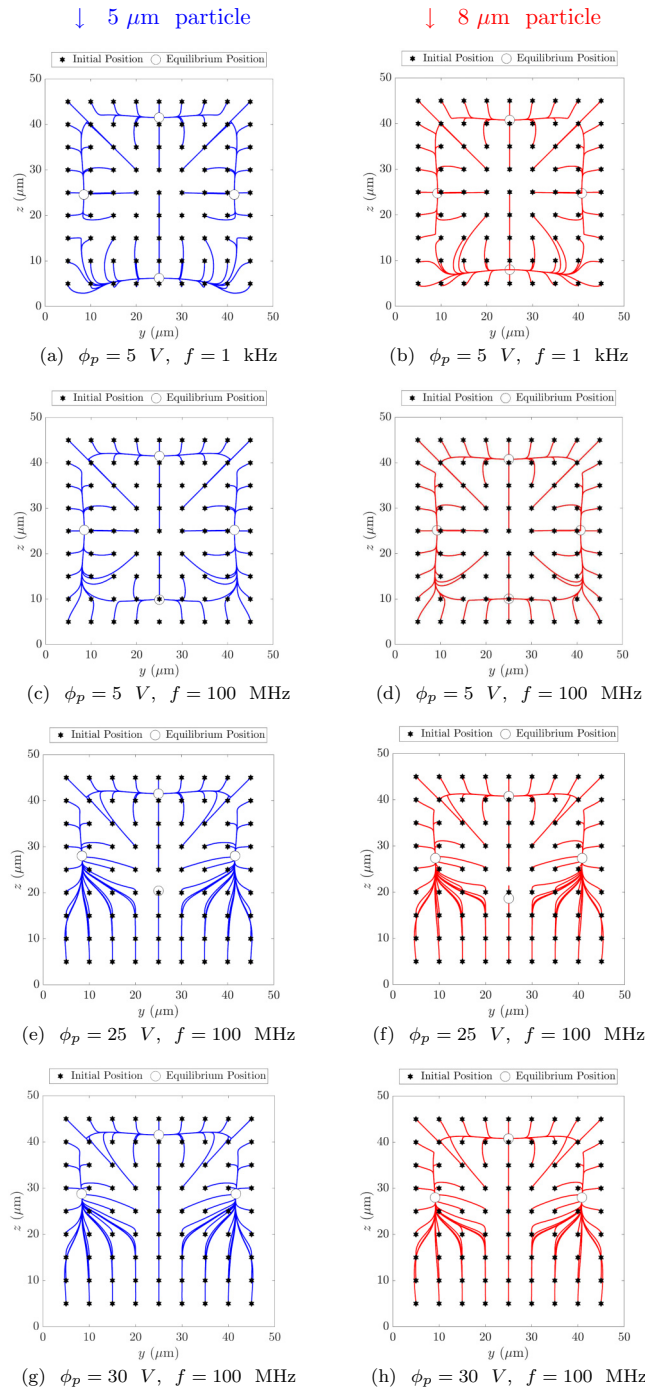
FIG. 6. Effect of dielectrophoretic force on the number and location of inertial equilibrium positions for the 5 μm (left) and 8 μm (right) polystyrene particles. At a low frequency (1 kHz), the polystyrene microparticles experience a positive dielectrophoretic force. Using a voltage of 5 V at the electrodes located at the bottom wall, the equilibrium position corresponding to the bottom wall approaches the electrodes, where the upward net lift force balances the downward dielectrophoretic force (a, b). At a high frequency (100 MHz), the particles experience a negative dielectrophoretic force. A voltage of 5 V at the electrodes, located at the bottom wall, displaces the equilibrium position from electrodes to the position where the downward net lift force balances the upward dielectrophoretic force (c, d). By increasing the voltage at the high frequency, the equilibrium distance from electrodes increases (e, f).

Here a two-step mechanism is presented to separate the microparticles. The steps are schematically demonstrated in Fig. 8. In the first step, electrodes are located at the top and bottom walls of the microchannel, while in the second step, electrodes are located at the side walls of the microchannel. The microelectrodes are configured in this way to provide more degrees of freedom in separation. In each step, a specific particle manipulation can be applied with no interference from the electrodes of the other step. In the first separation step, a strong negative dielectrophoretic force is generated from the electrodes located at the top and bottom walls of the microchannel, which leads to the migration of all particles to the inertial equilibrium positions corresponding to the microchannel side walls. At the end of the first separation step, the equilibrium positions corresponding to the top and bottom walls are free from particles.

In the second step, by setting the frequency to the crossover frequency of the nontarget particles, only target particles are affected by the negative dielectrophoretic force. In this case, using a high voltage which displaces target particles to the equilibrium positions corresponding to the top and bottom walls, target particles leave the microchannel through outlet 2 in Fig. 8 at the end of the separation. In contrast, nontarget particles leave the microchannel through outlets 1 and 3.

The proposed method has many advantages over the current microfluidics particle manipulation methods. This method is based on the negative dielectrophoresis such that particles are not exposed to the strong electric fields near the electrodes. This is especially important for bioparticles, where prolonged exposure to the strong electric fields leads to cell damage. Conventional microparticle manipulation devices that hinge upon inertial effects are not easily controllable. In contrast, our proposed method synergistically exploits both the dielectrophoretic and inertial forces; thus, the performance of the inertial forces can be modulated by the voltage and frequency of the applied electric field. In addition, the prefocusing of particles with the aid of a sheath flow is not required, which avoids the possibility of any external contamination.

In the following, the presented method is used to separate particles in two challenging mixtures: same-type particles of different sizes and same-size particles of different types.

1. Same-type particles of different sizes

The functionality of the proposed mechanism to separate different-sized microparticles is explored in this section. The periodic boundary condition was considered in the flow direction. Figure 9(a) depicts the configuration of the electrodes in one simulated period of the first separation step. Figure 9(b) also demonstrates the distribution of nondimensional electric potential in the periodic domain generated from electrodes at the top and bottom walls of the first step of the separation system. Figure 9(c) depicts the cross-sectional position of

At a threshold voltage particle passes the channel centerline where the change occurs in the direction of the shear-induced lift force, and the particle migrates to the original equilibrium position corresponding to the top wall (g, h).
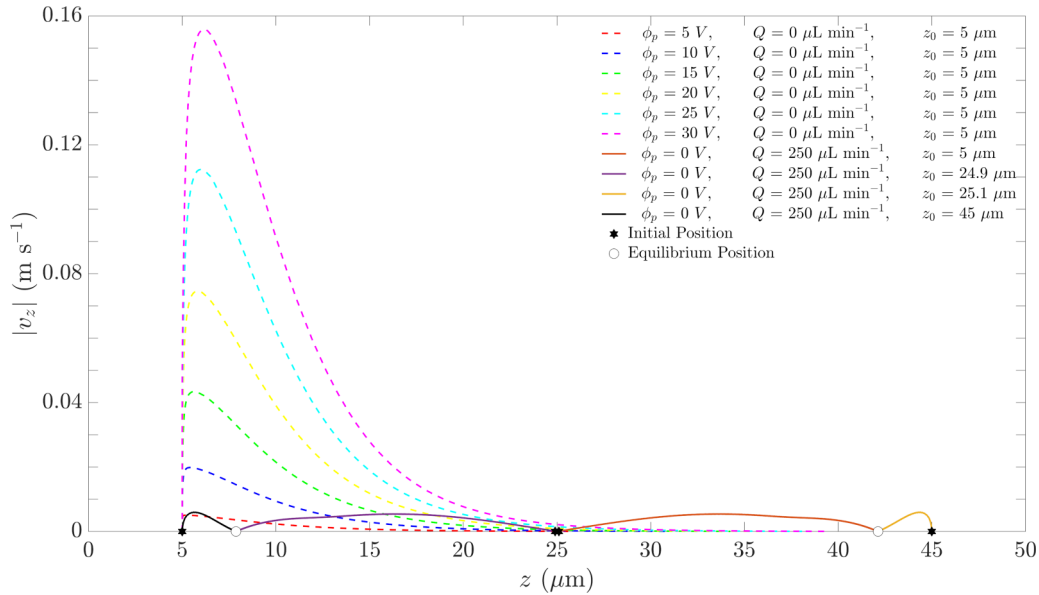
FIG. 7. Dielectrophoretic and inertial migration velocities as a function of vertical distance from electrodes located at the bottom wall ($z = 0\,\mu m$) for a 5 μm particle initially located at $y = 25\,\mu m$.

two 5 μm and two 8 μm polystyrene particles as a function of time in the first separation step. Based on the phenomenon observed in the preceding section, the voltage of 30 V and the frequency of 100 MHz generates a negative dielectrophoretic force, which can remove equilibrium positions near electrodes. According to Fig. 9(c), as time passes, all particles gradually migrate to the equilibrium positions corresponding to the side walls.

Figure 9(d) depicts the configuration of the electrodes in one simulated period of the second separation step. Figure 9(e) demonstrates the distribution of nondimensional electric potential in the periodic domain generated from electrodes at the left and right walls in the second step of the separation system. Figure 9(f) shows the position of the particles as a function of time in the second separation step. At the frequency of 200 kHz and voltage of 30 V, two 8 μm particles migrate to the equilibrium positions of the top and bottom walls, while two 5 μm particles are slightly displaced in their position as 200 kHz is close to the crossover frequency of 5 μm particles where they experience almost zero dielectrophoretic force.

2. Same-sized particles of different types

Another kind of particle mixture that is challenging to separate is the mixture of same-size particles with different types [14]. The separation of 6 μm MDA-231 CTCs from the same-size lymphocytes (WBCs) was simulated to demonstrate the ability of the proposed method to separate these challenging particles. In the first separation step, two WBCs and two CTCs are randomly distributed in the microchannel cross section. Figure 5(b) depicts the real part of the Clausius-Mossotti factor for these cells as a function of applied frequency. The frequency of 10 kHz was used in the first separation step. The use of a 30 V voltage leads to a negative dielectrophoretic force. According to Fig. 10(a), all particles migrate to the equilibrium positions corresponding to the microchannel side walls. Figure 10(b) demonstrates the migration of cells in the second separation step. At the frequency of 80 kHz, close to the crossover frequency of CTCs, a negative dielectrophoretic force is formed, which displaces WBCs to the equilibrium positions corresponding to the top and bottom walls while CTCs remain in the equilibrium positions close to the side walls. Following the second step, CTCs leave the microchannel from outlets 1 and 3 in Fig. 8, whereas WBCs leave the microchannel at outlet 2.

V. CONCLUSION

The dynamics of microparticles were simulated in a straight microchannel with a square cross section. A hybrid dielectrophoresis-assisted inertial microfluidic method was presented for microparticle separation. The immersed boundary and lattice Boltzmann methods were implemented on a single GPU. AA pattern of storing distribution functions on memory was used to overcome the issue of limited memory of the GPU, making it possible to perform fast and detailed simulations. Particles immersed in the fluid flow migrated towards four stable positions depending on their initial

FIG. 8. Schematic representation of the proposed two-step dielectrophoretic-controlled inertial microfluidic separation method. In the first step, electrodes are located at the top and bottom walls, while electrodes are located at the side walls in the second step.
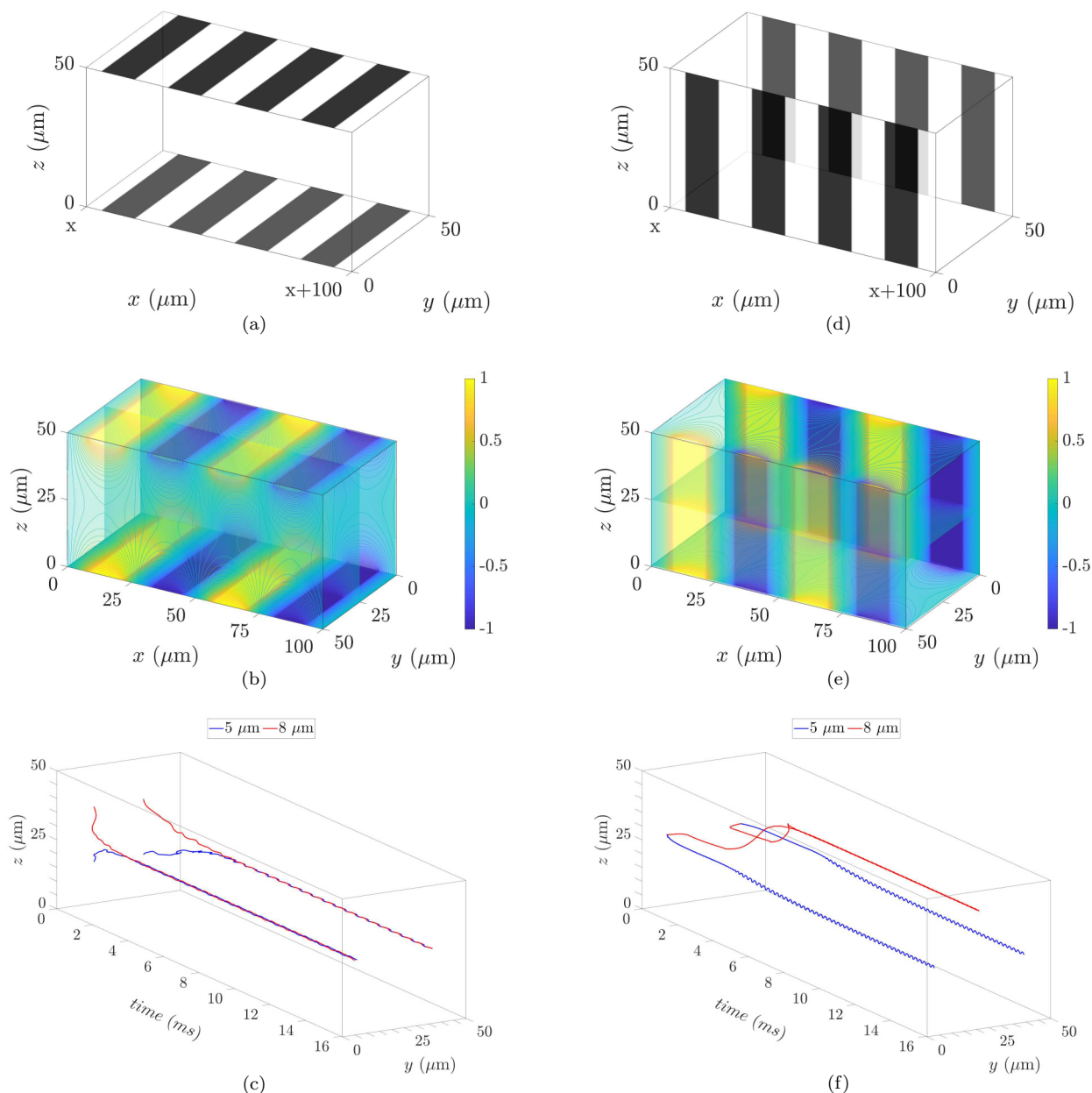
FIG. 9. Configuration of electrodes in one simulated period of the first separation step (a), electric-potential distribution in one period of the first step (b), and the migration of 5 and 8 μm polystyrene particles to the inertial equilibrium positions corresponding to the side walls as a function of time in the first separation step (c). Configuration of electrodes in one simulated period of the second separation step (d), electric-potential distribution in one period of the second step (e), and the migration of 8 μm polystyrene particles to the inertial equilibrium positions corresponding to the top and bottom walls as a function of time in the second separation step (f).

positions. The dielectrophoretic force was utilized to manipulate the location and number of these equilibrium positions. At a threshold voltage, the negative dielectrophoretic force made the equilibrium position near the electrodes pass the channel centerline and merge with other equilibrium positions far from the electrodes.

This particle separation method comprises two steps. The first step involves the application of a specific frequency on the electrodes implemented at the top and bottom walls such that all particles experience a negative dielectrophoretic force. Using a high voltage (greater than the threshold voltage of all microparticles), all microparticles migrate to the

equilibrium positions corresponding to the microchannel side walls. In the second step, a frequency close to the crossover frequency of one set of particles is applied at the electrodes implemented at the side walls (the Clausius-Mossotti factor for the other set of particles is negative). Using a high voltage (greater than the threshold voltage of particles that are intended to be displaced), particles that experience a strong negative dielectrophoretic force migrate to the equilibrium positions corresponding to the top and bottom walls; while no significant variation occurs in the equilibrium positions of other particles. This approach benefits from the advantages of both active and passive microfluidic separation
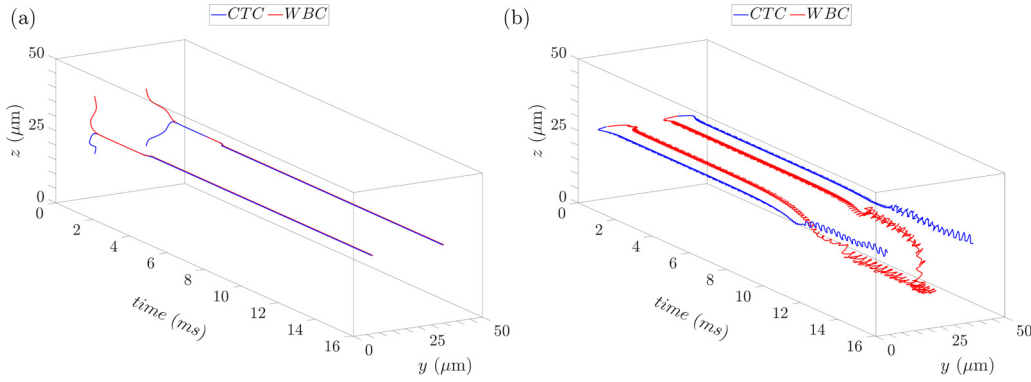
FIG. 10. Migration of CTCs and WBCs to the inertial equilibrium positions corresponding to the side walls in the first separation step (a). Migration of WBCs to the inertial equilibrium positions corresponding to the top and bottom walls in the second separation step (b).

methods while avoiding their limitations, thus, offering a high-throughput and controllable separation approach. The applicability of the proposed mechanism was demonstrated by numerical simulation of the separation in two challenging mixtures: different-sized polystyrene microparticles and the CTCs-WBCs mixtures.

APPENDIX A: THE SIMULATION ALGORITHM

The simulation algorithm consists of two parts. The first one is solving the Poisson equation, which is demonstrated in Fig. 11 as blue-colored blocks. The second part is the simulation of fluid-particle interaction in the presence of dielectrophoretic force using the immersed boundary–lattice Boltzmann method, which is represented in Fig. 11 as orange-colored blocks. The first part starts with initializing the electric potential ϕ and distribution functions g_i. At the start of each simulation, electric potential is set to zero throughout the computational domain. Also, distribution functions are set to zero, which is the equilibrium value corresponding to the zero potential according to Eq. (23).

In the collision step, distribution functions associated with the point $\mathbf{x}$ of the computational domain at time t are read from 19×8 bytes of memory corresponding to the same fluid point $\mathbf{x}$ according to Fig. 12(a). After that, postcollision distribution functions are calculated using Eq. (27). Postcollision distribution functions are stored in the corresponding memory of the same fluid point $\mathbf{x}$ according to Fig. 12(b). All distribution functions that propagate to the boundary nodes are calculated using the postcollision form of the nonequilibrium extrapolation method [Eq. (33)].

To perform the propagation-collision-propagation step, distribution functions are read from the 19×8 bytes of memory corresponding to the fluid node $\mathbf{x} - \mathbf{e_i} \Delta \tilde{t}$ according to Fig. 12(b), which is equivalent to the first propagation. Postcollision distribution functions are calculated using Eq. (27) and stored in consecutive 19×8 bytes of memory corresponding to the fluid point $\mathbf{x} + \mathbf{e_i} \Delta \tilde{t}$ according to Fig. 12(a), which is equivalent to the second propagation. All distribution functions at the boundary nodes are calculated using the postpropagation form of the nonequilibrium extrapolation method [Eq. (32)]. Simulation is continued until the steady-state solution of Eq. (19) is attained, which is the electric potential distribution in the computational domain. Then the distribution of electric field is calculated using Eq. (5) from the electric potential.

In order to perform fluid-structure interaction, the surface of each spherical particle should be partitioned. The algorithm proposed by Beckers *et al.* [39] is used to partition the surface of spherical particles into equal-area segments of unit aspect ratio, with immersed boundary nodes being located at the center of each segment. Figures 13(a) and 13(b) depict how two different-sized particles are partitioned.

The second part of the simulation algorithm starts with the initialization of fluid velocity $\mathbf{u}$, density ρ, and distribution functions f_i. The fluid velocity is set to zero at the start of the simulation throughout the simulation domain. The value of density at the computational nodes is set to the fluid density ρ_f. Distribution functions are set to their corresponding
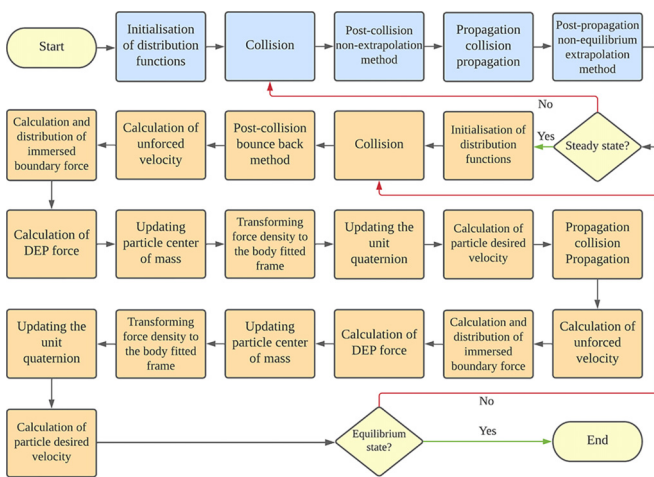
FIG. 11. The simulation algorithm of inertial migration in an oscillating electric field. Blue-colored blocks represent the lattice Boltzmann method for solving the Poisson equation. Orange-colored blocks represent the immersed boundary-lattice Boltzmann method for simulation of fluid-particle interaction in the presence of dielectrophoretic force.

(a)

f_0	f_1	f_2	f_3	f_4	f_5	f_6	f_7	f_8	f_9	f_{10}	f_{11}	f_{12}	f_{13}	f_{14}	f_{15}	f_{16}	f_{17}	f_{18}

(b)

f_0	f_2	f_1	f_4	f_3	f_6	f_5	f_8	f_7	f_{10}	f_9	f_{12}	f_{11}	f_{14}	f_{13}	f_{16}	f_{15}	f_{18}	f_{17}
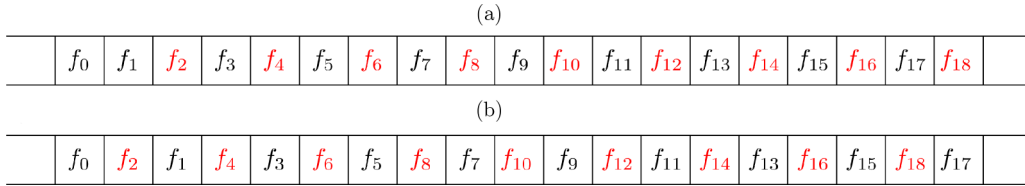
FIG. 12. Order of saving distribution functions in memory using AA pattern after propagation-collision-propagation (a) and collision (b) steps.

equilibrium values, which are calculated using Eq. (14). In the collision step, distribution functions associated with the point **x** of the fluid domain at time t are read from 19×8 bytes of memory corresponding to the fluid point **x** according to Fig. 12(a). After that, postcollision distribution functions are calculated using Eq. (26). Postcollision distribution functions are stored in the corresponding memory of the same fluid node **x**, according to Fig. 12(b). Unknown distribution functions propagated into the computational domain at the boundary nodes are calculated using the postcollision form of the bounce-back method [Eq. (31)].

The desired fluid velocity required for the immersed boundary force calculation at the particle surface is calculated using Eq. (47). The unforced velocity is calculated using the postpropagation distribution functions. In this regard, distribution functions of fluid node **x** are read from the memory corresponding to the point $\mathbf{x} - \mathbf{e}_i \Delta t$ according to Fig. 12(b). Unforced velocity at the lattice nodes is calculated using Eq. (18) by setting $\mathbf{f} = \rho \mathbf{g}_d$. The unforced velocity is interpolated at the location of each boundary node $\mathbf{x}_s$ using Eq. (49). According to Eq. (51), 64 fluid nodes are engaged in the calculation and spreading of the immersed boundary force at each boundary node, such that one block of 64 threads [40] has been used for the corresponding calculations of each immersed boundary node. The summation in Eq. (49) is calculated using the parallel reduction method [40]. The immersed boundary surface force density $\mathbf{F}_s$ is calculated using Eq. (46) at the location of immersed boundary nodes $\mathbf{x}_s$. Then each thread calculates the share of its corresponding fluid node, $\mathbf{F}_s(\mathbf{x}_s, t)D(\mathbf{x} - \mathbf{x}_s)\Delta S$, from the calculated surface force density and adds it to the $\mathbf{F}_b$ value of that node. The addition is performed using the GPU function *atomicAdd*(). This function temporarily stops the operation of other threads until the task of the current thread is completed, which removes the possibility of interference when two threads from different blocks

are writing to the same location in memory at the same time [41].

The dielectrophoretic force acting on the particle is calculated using Eq. (2). The value of $\nabla |\mathbf{E}_{rms}|^2$ is interpolated at the particle center of mass from the steady-state solution of the Poisson equation calculated in the first part of the simulation algorithm. Dielectrophoretic and hydrodynamic forces update particle linear and angular velocities using Eqs. (38) and (42), respectively. After that, the position and orientation of the particle are updated using Eqs. (39) and (43), respectively.

To perform the propagation-collision-propagation step, distribution functions are read from the 19×8 bytes of memory corresponding to the fluid node $\mathbf{x} - \mathbf{e}_i \tilde{t}$, according to Fig. 12(b), which is equivalent to the first propagation. By using the calculated immersed boundary force, postcollision distribution functions are calculated using Eq. (26). After that, postcollision distribution functions are stored in consecutive 19×8 bytes of memory corresponding to the fluid point $\mathbf{x} + \mathbf{e}_i \tilde{t}$, according to Fig. 12(a), which is equivalent to the second propagation. Unknown distribution functions, propagated into the computational domain at the boundary nodes, are calculated using the postpropagation form of the bounce-back method [Eq. (30)].

To calculate the unforced velocity, distribution functions of fluid node **x** are read from the consecutive 19×8 bytes of memory corresponding to the fluid node **x** according to Fig. 12(a). Unforced fluid velocity at the fluid nodes is calculated using Eq. (18) by setting $\mathbf{f} = \rho \mathbf{g}_d$. Then the unforced velocity is interpolated at each immersed boundary node $\mathbf{x}_s$ using Eq. (49). The configuration of GPU blocks and threads is the same as the former immersed boundary force calculation. The calculated immersed boundary force [using Eq. (46)] and the calculated dielectrophoretic force at the particle center [using Eq. (2)] are used to update the linear and angular velocities of particle using Eqs. (38) and (42), followed by
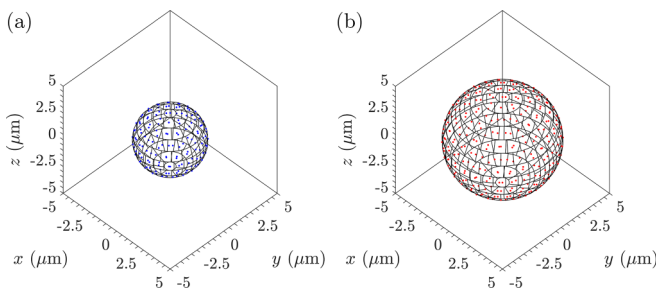
FIG. 13. Partitioning the 5 μm particle surface into 165 equal area and unit aspect ratio segments (a) and the 8 μm particle surface into 295 equal area and unit aspect ratio segments (b). Boundary nodes are located at the center of the segments.
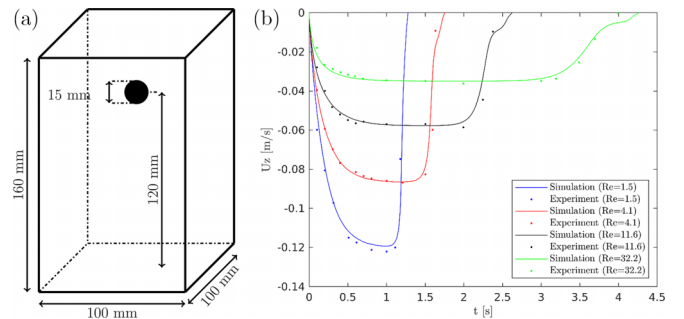
FIG. 14. Schematic representation of the computational domain of the single sphere sedimentation due to the gravity (a), and settling velocity of the single sphere in four different types of silicone oil (b).

TABLE I. Simulation parameters and properties of silicone oils used in the particle sedimentation problem.

Case no.	Density (kg m^{-3})	Viscosity (10^{-3} kg m^{-1} s^{-1})	Reynolds number
1	970	373	1.5
2	965	212	4.1
3	962	113	11.6
4	960	58	32.2

the linear and angular motion of particle using Eqs. (39) and (43).

APPENDIX B: VALIDATION OF THE NUMERICAL METHODS

The validity of the developed parallel immersed boundary–lattice Boltzmann code is examined by simulating the sedimentation of a single spherical particle in four different types of silicone oil, and the simulation results are compared with experimental data from the literature [42]. As shown in Fig. 14(a), a spherical particle with diameter 15 mm and density 1120 kg m^{-3} is initially located at the height of 120 mm in a cuboid of size *depth* × *width* × *height* = 100 mm × 100 mm × 160 mm. At the beginning of the experiment, the particle starts settling in the fluid. Simulation parameters and the properties of the silicon oils are shown in Table I. Figure 14(b) represents the settling velocity of the particle as a function of time. It is observed that there is a reasonable agreement between simulation results and experimental data.

To ensure that our developed solver can accurately resolve the microscale fluid-structure interaction phenomena, the migration of a 10 μm particle in a square cross-sectional microchannel of height H (= 50 μm) is also simulated, and the results are compared with those reported by Lashgari *et al.* [43]. In this simulation, the Reynolds number based on the bulk flow velocity and hydraulic diameter is set to 100. Figure 15 represents the migration of 10 μm particle in the upper half of the microchannel. It is observed that the particle trajectory and the final equilibrium position (0.2H away from the top wall) well agree with those reported in
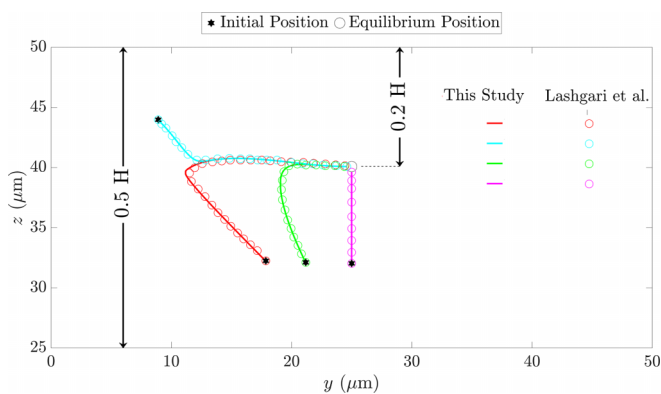
FIG. 15. Comparison between the results of this study and those reported in [43] for the migration of the 10 μm particle in the cross section and inertial equilibrium position (0.2 H from the top wall).
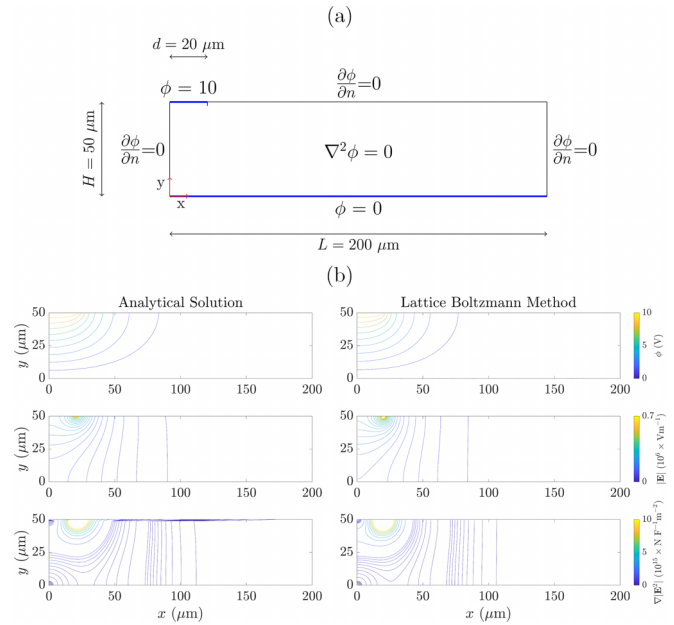
FIG. 16. Geometry and boundary conditions of the dielectrophoresis validation problem (a), and comparison between analytical and numerical values of electric potential, electric field and dielectrophoretic force in the domain of panel (a) and (b).

[43], which further confirms the accuracy of the developed immersed boundary–lattice Boltzmann code.

Moreover, we have provided another validations in the main text. That was the two-stage migration of particles to the inertial equilibrium positions, which has already been published [35]. These validations guarantee that our developed code accurately simulates the fluid-structure interaction phenomena in microfluidic systems.

To validate the developed lattice Boltzmann Poisson solver and the dielectrophoretic force calculation method, the Laplace equation [Eq. (8)] has been solved for the domain of Fig. 16(a), and the analytical and numerical values of electric potential, electric field, and dielectrophoretic force are compared. The boundary conditions in the x and y directions are shown in Fig. 16(a). The analytical solutions are calculated using the Fourier series and separation of variable method [44].

In the numerical simulation using the lattice Boltzmann method, periodic boundary conditions in the z direction perpendicular to the plane has been used, which means that the solution of the 2D problem has been calculated with the developed 3D solver. This problem has been chosen as the validation problem of the proposed dielectrophoretic force calculation method because it contains Dirichlet, Neumann, and periodic boundary conditions that have been appeared in this study. Dirichlet and Neumann boundary conditions are enforced using the nonequilibrium extrapolation method. The lattice spacing is chosen to be $\Delta x = 0.5$ μm. Figure 16(b) represents the contours plots of electric potential, electric field, and dielectrophoretic force. It is observed that there is a reasonable agreement between the analytical and numerical solutions.

TABLE II. Dielectric properties of lymphocyte (WBC) and MDA-231 (CTC) [14].

Property	Lymphocyte	MDA-231
r_p (µm)	6	6
d (nm)	7	4
σ_{mem} (S m^{-1})	1.4×10^{-7}	1×10^{-6}
$\epsilon_{\text{mem}}/\epsilon_0$	12.8	11.75
σ_{int} (S m^{-1})	0.83	0.62
$\epsilon_{\text{int}}/\epsilon_0$	73.2	52

APPENDIX C: CALCULATION OF THE CLAUSIUS-MOSSOTTI FACTOR

1. Polystyrene microparticles

The electrical conductivity of spherical polystyrene microparticles is expressed as a function of the particle radius as [45]

$$\sigma_p = \sigma_{\text{bulk}} + \frac{2K_s}{r_p}, \tag{C1}$$

where K_s (= 2 nS), and σ_{bulk} (= 10^{-14} S m^{-1}) are the surface conductance and the bulk conductivity of the polystyrene

microparticles, respectively. The conductivity and permittivity of the deionized water as the medium are, respectively, 1.5×10^{-4} S m^{-1} and $78\,\epsilon_0$, where ϵ_0 (= 8.854×10^{-12} F m^{-1}) is the vacuum permittivity [46]. Equation (C1), in combination with Eqs. (3) and (4), is used to calculate the Clausius-Mossotti factor of different-sized polystyrene microparticles.

2. Bioparticles

To characterize the dielectric behavior of bioparticles, the single-shell model is used in which the effective complex permittivity of the cell is expressed as [47]

$$\epsilon_{\text{cell}}^* = \frac{\left(\frac{r_p}{r_p-d}\right)^3 + 2\left(\frac{\epsilon_{\text{int}}^* - \epsilon_{\text{mem}}^*}{\epsilon_{\text{int}}^* + 2\epsilon_{\text{mem}}^*}\right)}{\left(\frac{r_p}{r_p-d}\right)^3 - \left(\frac{\epsilon_{\text{int}}^* - \epsilon_{\text{mem}}^*}{\epsilon_{\text{int}}^* + 2\epsilon_{\text{mem}}^*}\right)}, \tag{C2}$$

where r_p is the radius of the cell, and d is the membrane thickness. ϵ_{mem}^*, and ϵ_{int}^* are the complex permittivity of membrane and cytoplasm, respectively. σ_{mem}, and σ_{int} are the electrical conductivity of membrane and cytoplasm, respectively. The conductivity and permittivity of the medium is considered to be 0.055 S m^{-1} and $78\,\epsilon_0$, respectively. The dielectric parameters for the cells used in this study are given in Table II.

[1] Y. Gao, W. Li, and D. Pappas, Analyst **138**, 4714 (2013).

[2] D. Di Carlo, J. F. Edd, D. Irimia, R. G. Tompkins, and M. Toner, Anal. Chem. **80**, 2204 (2008).

[3] J. C.-T. Lin, D.-J. Lee, and C. Huang, Separat. Sci. Tech. **45**, 858 (2010).

[4] P. Sajeesh and A. K. Sen, Microfluid. Nanofluid. **17**, 1 (2014).

[5] S. Yan, J. Zhang, D. Yuan, and W. Li, Electrophoresis **38**, 238 (2017).

[6] T. Kiryo, Y. Takahashi, and S. Miyata, Eng. Life Sci. **22**, 417 (2022).

[7] A. Atajanov, A. Zhbanov, and S. Yang, Micro Nano Syst. Lett. **6**, 2 (2018).

[8] D. Radziuk and H. Möhwald, Phys. Chem. Chem. Phys. **18**, 21 (2016).

[9] V. Gupta, I. Jafferji, M. Garza, V. O. Melnikova, D. K. Hasegawa, R. Pethig, and D. W. Davis, Biomicrofluidics **6**, 024133 (2012).

[10] A. Rahmani, A. Mohammadi, and H. R. Kalhor, Electrophoresis **39**, 445 (2018).

[11] L. Wang, J. Lu, S. A. Marchenko, E. S. Monuki, L. A. Flanagan, and A. P. Lee, Electrophoresis **30**, 782 (2009).

[12] J. Zhang, D. Yuan, Q. Zhao, S. Yan, S.-Y. Tang, S. H. Tan, J. Guo, H. Xia, N.-T. Nguyen, and W. Li, Sensors Actuators B **267**, 14 (2018).

[13] J. Zhang, S. Yan, G. Alici, N.-T. Nguyen, D. Di Carlo, and W. Li, RSC Adv. **4**, 62076 (2014).

[14] M. Khan and X. Chen, Electrophoresis **43**, 879 (2022).

[15] P. Bailey, J. Myre, S. D. Walsh, D. J. Lilja, and M. O. Saar, in *2009 International Conference on Parallel Processing* (IEEE, New York, 2009), pp. 550–557.

[16] G. Segre and A. Silberberg, J. Fluid Mech. **14**, 115 (1962).

[17] G. Segre and A. Silberberg, J. Fluid Mech. **14**, 136 (1962).

[18] J. Zhang, S. Yan, D. Yuan, G. Alici, N.-T. Nguyen, M. E. Warkiani, and W. Li, Lab Chip **16**, 10 (2016).

[19] B. Ho and L. Leal, J. Fluid Mech. **65**, 365 (1974).

[20] S. R. Bazaz, A. Mashhadian, A. Ehsani, S. C. Saha, T. Krüger, and M. E. Warkiani, Lab Chip **20**, 1023 (2020).

[21] C. Rosales and K. M. Lim, Electrophoresis **26**, 2057 (2005).

[22] R. R. Pethig, *Dielectrophoresis: Theory, Methodology and Biological Applications* (John Wiley & Sons, New York, 2017).

[23] A. Mohammadi, Transp. Porous Media **104**, 469 (2014).

[24] T. Krüger, H. Kusumaatmaja, A. Kuzmin, O. Shardt, G. Silva, and E. M. Viggen, *The Lattice Boltzmann Method* (Springer International Publishing, Cham, 2017).

[25] K. Luo, J. Wu, H.-L. Yi, and H.-P. Tan, Int. J. Heat Mass Transf. **103**, 832 (2016).

[26] Z. Guo, C. Zheng, and B. Shi, Phys. Rev. E **65**, 046308 (2002).

[27] T. Seta, Phys. Rev. E **87**, 063304 (2013).

[28] A. J. Ladd, J. Fluid Mech. **271**, 285 (1994).

[29] G. Zhao-Li, Z. Chu-Guang, and S. Bao-Chang, Chin. Phys. **11**, 366 (2002).

[30] Z.-G. Feng and E. E. Michaelides, Comput. Fluids **38**, 370 (2009).

[31] T. Pöschel and T. Schwager, *Computational Granular Dynamics: Models and Algorithms* (Springer Science & Business Media, Heidelberg, 2005).

[32] Z.-G. Feng and E. E. Michaelides, J. Comput. Phys. **195**, 602 (2004).

[33] S. K. Kang and Y. A. Hassan, Int. J. Numer. Methods Fluids **66**, 1132 (2011).

[34] B. E. Rapp, *Microfluidics: Modeling, Mechanics and Mathematics* (William Andrew, Norwich, NY, 2016).

[35] J. Zhou and I. Papautsky, Lab Chip **13**, 1121 (2013).

[36] B. Owen and T. Krüger, J. Fluid Mech. **937**, A4 (2022).

[37] R. C. Coelho, D. P. Silva, A. M. Maschio, M. M. Telo da Gama, and N. A. Araújo, Phys. Fluids **35**, 013304 (2023).

[38] R. B. Bird, Appl. Mech. Rev. **55**, R1 (2002).

[39] B. Beckers and P. Beckers, Comput. Geom. **45**, 275 (2012).

[40] J. Sanders and E. Kandrot, *CUDA by Example: An Introduction to General-Purpose GPU Programming* (Addison-Wesley Professional, New York, 2010).

[41] J. Cheng, M. Grossman, and T. McKercher, *Professional CUDA C Programming* (John Wiley & Sons, New York, 2014).

[42] A. Ten Cate, C. Nieuwstad, J. Derksen, and H. Van den Akker, Phys. Fluids **14**, 4012 (2002).

[43] I. Lashgari, M. N. Ardekani, I. Banerjee, A. Russom, and L. Brandt, J. Fluid Mech. **819**, 540 (2017).

[44] A. Alazzam, D. Roman, V. Nerguizian, I. Stiharu, and R. Bhat, Microfluid. Nanofluid. **9**, 1115 (2010).

[45] Q. Chen and Y. J. Yuan, RSC Adv. **9**, 4963 (2019).

[46] S. H. Baek, W.-J. Chang, J.-Y. Baek, D. S. Yoon, R. Bashir, and S. W. Lee, Anal. Chem. **81**, 7737 (2009).

[47] D. Kim, M. Sonker, and A. Ros, Anal. Chem. **91**, 277 (2019).